applied sciences

MDPI

Article

Eccentric Compression Behavior of Coral Aggregate Geopolymer Concrete Columns Reinforced with Stainless-Steel Rebars

Haiwen Xu [1,2,*], Jiasheng Jiang [3] and Chao Yang [1,2]

[1] State Key Laboratory of Featured Metal Materials and Life-Cycle Safey for Composite Structure, Guangxi University, Nanning 530004, China; 15123893082@163.com
[2] Guangxi Key Laboratory of Disaster Prevention and Structural Safety, College of Civil Engineering and Architecture, Guangxi University, Nanning 530004, China
[3] College of Civil Engineering and Architecture, Nanning University, Nanning 541699, China; 2010401006@st.gxu.edu.cn
* Correspondence: xuhaiwen2000@163.com

Abstract: Using coral aggregates instead of natural aggregates can save both raw material transportation costs and time in island construction projects. However, coral aggregates are characterized by high brittleness, low strength, and a high chloride content, which result in the brittleness and durability of coral aggregate concrete (CAC). On the other hand, carbon emissions are prominent in the production of Portland cement. A reinforced concrete structure composed of a stainless-steel rebar (SSR), geopolymer concrete, and coral aggregate was employed to address these challenges. Considering that columns are commonly used structural elements, this paper investigates the eccentric compression behavior of stainless-steel rebar-reinforced coral aggregate geopolymer concrete columns (SCGCs) by varying eccentricity (e_0 = 70, 140, 210, and 280 mm) and reinforcement ratio (ρ_s = 0.302%, 0.536%, and 0.838%) values. The failure patterns, load–deformation curves, and crack development of SCGCs were obtained. These results indicate that the failure pattern of SCGCs under eccentric compression is similar to that of conventional reinforced concrete columns. However, SCGCs exhibited a greater lateral deformation. A refined load-bearing capacity prediction model for SCGCs was developed by integrating the constitutive model of coral aggregate geopolymer concrete (CAGC). Furthermore, a crack width prediction model specifically suited for SCGCs was developed, considering the differences in the bond performance between CAGCs and the SSR compared to ordinary concrete and carbon steel and the characteristic of the SSR lacking a yield plateau. The calculations using the refined load-bearing capacity prediction model and the crack width prediction model fit well with the experimental results, indicating that these two models have good application prospects.

Keywords: coral aggregate geopolymer concrete; stainless-steel rebar; eccentric compression; bearing capacity; crack width

Academic Editor: Muhammad Junaid Munir

Received: 19 February 2025
Revised: 15 March 2025
Accepted: 16 March 2025
Published: 25 March 2025

Citation: Xu, H.; Jiang, J.; Yang, C. Eccentric Compression Behavior of Coral Aggregate Geopolymer Concrete Columns Reinforced with Stainless-Steel Rebars. *Appl. Sci.* **2025**, *15*, 3570. https://doi.org/10.3390/app15073570

1. Introduction

The large-scale development of island engineering projects is underway, driven by the rapid expansion of the marine industry [1]. However, constructing these island projects requires a substantial amount of building materials, and transporting these materials from inland is both time-consuming and expensive [2]. Comprehensive studies have shown that collecting and utilizing coral reef debris does not adversely affect marine ecosystems [3]. This approach, which involves the use of crushed and screened coral reef debris to replace

gravel and seawater instead of fresh water, can effectively mitigate the environmental impact of traditional construction materials while also reducing transportation and time costs during construction [4]. To date, many scholars have validated the feasibility of using coral aggregate concrete (CAC) in island engineering projects, with the research focusing on the mechanical properties [5,6], shrinkage [7], bonding performance [8], and durability [9] of CAC.

However, coral aggregate has drawbacks, such as high porosity (15–45%), a high chloride ion content, and low strength (0.6–2.1 MPa) [10,11]. Under the same water–cement ratio, the strength and durability of CAC are lower than those of Ordinary Portland Cement (OPC) concrete. Moreover, the apparent chloride ion diffusion coefficient (D_a) of CAC is 1 to 8 times higher than that of OPC, and its total free chloride ion content (C_f) is significantly greater than that of OPC [12]. As a result, the corrosion of reinforcement within CAC structures is more severe than in OPC structures when used in island construction projects. It is also noteworthy that two drawbacks limiting its potential as an environmentally friendly material are that the production of Portland cement consumes a large amount of energy and emits significant quantities of CO_2. According to the statistics, producing one ton of cement generates approximately 10 kg of dust, 2 kg of nitrogen oxides, 1 kg of sulfur dioxide, and other by-products [13]. Therefore, it is imperative to address the issue of reinforcement corrosion within CAC structures in marine environments and to seek more "green" alternatives for cementitious materials.

Geopolymer, as a novel and sustainable alternative cementitious material, primarily utilizes industrial waste materials, such as slag, fly ash, and metakaolin, making it an ideal substitute for traditional cement [14]. The combination of geopolymer concrete (GPC) with coral aggregate facilitates the formation of the C-S-H gel phase at the mortar matrix–coral aggregate interface, while the naturally dense pores of coral aggregate contribute to a tight interface transition zone with the cementitious material [15,16]. Thus, the incorporation of a geopolymer not only mitigates the carbon emissions issues associated with Portland cement, but also enhances the split tensile strength, axial compressive strength, and elastic modulus of CAC [17,18].

To prevent rebar corrosion, scholars have proposed various methods, such as applying surface coatings to concrete, increasing the thickness of the concrete cover, using high-performance concrete to block the penetration paths of corrosive agents, galvanizing the rebar, coating the rebar with epoxy resin, using corrosion inhibitors, and providing cathodic protection for the rebar.

However, the aforementioned measures cannot fundamentally solve the problem of steel corrosion, and those measures can only extend the service life of the structure by approximately 20 years [19]. Jing [20] studied the corrosion resistance of duplex stainless-steel rebars (SSRs) used for the Hong Kong Zhuhai Macao Bridge and demonstrated that the critical chloride ion concentration for the SSRs in simulated concrete pore solutions is 3.9 to 3.95 mol/L, which is about 60 times that of a carbon steel rebar. Da [21] found that the corrosion resistance of SSRs embedded in CAC is higher than that of carbon steel rebars with surface coatings, with carbon steel rebars performing the worst. In summary, the SSR exhibits excellent corrosion resistance, effectively addressing the problem of rebar corrosion. However, the mechanical properties of SSRs lead to differences in the structural behavior of stainless-steel rebar concrete (SSRC) structures compared to ordinary reinforced concrete (ORC) structures. The plasticity of the SSR results in greater deformation and wider cracks in SSRC structures during the service stage. Li [22] discovered through experiments that eccentrically loaded SSR columns develop wider cracks than carbon steel rebar columns with the same eccentricity and reinforcement ratio. The high ductility of SSRs causes differences in the load redistribution and stress redistribution patterns

in SSRC structures compared to ORC structures, and the asymmetry in the stress–strain curves of SSRs under tension and compression render existing load-bearing capacity calculation formulas unsuitable [19]. Scholars, such as Rabi [23,24], have pointed out that the load-bearing capacity calculation formulas proposed in Eurocode 2 are not applicable to SSRC beams.

In response, scholars have conducted extensive research on the mechanical behavior of SSRC structures. Li [25] found that the strain distribution in the cross-section of four-point bending SSRC beams adheres to the plane section assumption, and the failure pattern is similar to that of ORC beams. Rabi [26] proposed a continuous strength method based on the constitutive relationship of SSRs, which more accurately and reliably predicts the load-bearing capacity of SSRC structures. Khalifa [27] suggested using equivalent stress to replace the yield strength of duplex and austenitic SSRs to calculate the axial-flexural capacity. Building on this, Li [22] developed a computational model for predicting the N-M curves of SSRC columns. Additionally, scholars have also explored the fatigue performance [28] and seismic performance [29] of SSRC structures.

However, although extensive experimental studies and theoretical design studies have been conducted on SSRC structures, no studies have been reported on the eccentric compression behavior of SCGC columns. In addition, since columns are the basic components of frame structures, it is beneficial to study the mechanical properties of columns in depth, and thus it is crucial to study their eccentric compression behavior [30,31]. In this study, a novel concrete column structure that integrates geopolymers, CAC, and SSRs is proposed to further address the limitations of carbon steel reinforcement in marine structures. Considering that columns in real projects are usually subjected to eccentric loading, in this paper, eight SCGCs with different eccentricity (e_0) and reinforcement ratios (ρ_s) were tested with eccentric loading to examine the mechanical behavior of SCGCs under such conditions.

2. Experimental Program

2.1. Raw Material and Mix Ratio of Concrete

This study utilized coral fragments from the Philippines as coarse aggregates (Figure 1) and fine aggregates (Figures 2 and 3). The original coral coarse aggregate (CCA) contained a significant number of coral particles with diameters exceeding 20 mm. In this study, a jaw crusher was used for secondary crushing to prevent an excessive proportion of large-sized coral aggregates from affecting the development of concrete strength. The particle size of the crushed CCA ranged from 2.36 mm to 19 mm, as shown in Figure 4, which was determined based on the sieve analysis and material properties according to the standard JGJ51-2002 [32]. Table 1 presents the physical properties of the CCA.

Figure 1. Coarse coral aggregate.

Figure 2. Coarse coral sand.

Figure 3. Fine coral sand.

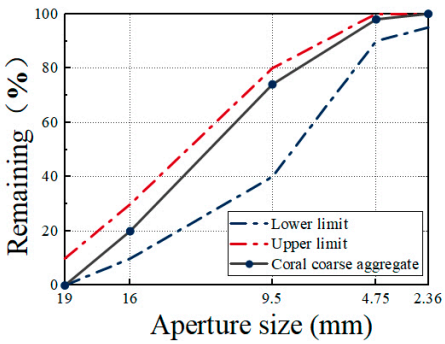

Figure 4. Gradation curve of coral coarse aggregate after crushing treatment.

Table 1. Basic properties of coral coarse aggregate.

No.	1 h Water Absorption (%)	24 h Water Absorption (%)	Bulk Density (kg/m^3)	Apparent Density (kg/m^3)	Cylinder Compressive Strength (MPa)	Silt Content (%)
Coral coarse aggregate	7.82	8.13	882	2092	2.1	4.2

In this study, coral coarse sand and coral fine sand were mixed in a 1:1 mass ratio to obtain mixed coral sand, which helps avoid the issue of a single type of coral sand leading to poor gradation, which can be detrimental to the development of concrete strength. The particle size distribution of the mixed coral sand was analyzed, and its material properties were measured in accordance with standards GB/T17431-2010 [33] and JGJ52-2006 [34]. The relevant parameters are presented in Figure 5 and Table 2. The blended coral sand was classified as a lightweight aggregate, with a fineness modulus of 3.0, falling into the medium sand zone II, and had a continuous grading.

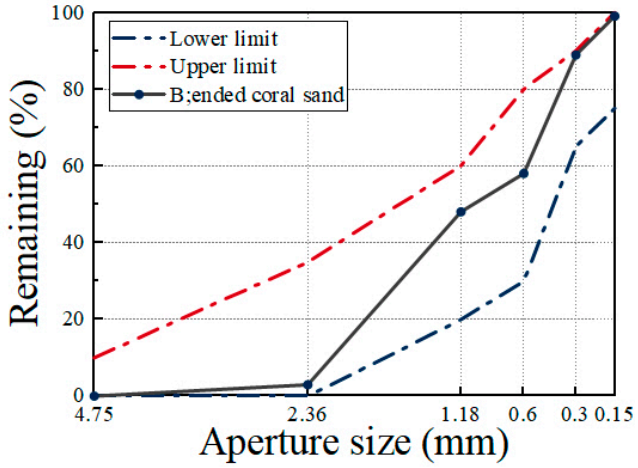

Figure 5. Gradation curve of mixed coral sand.

Table 2. Basic properties of mixed coral sand.

No.	1 h Water Absorption (%)	24 h Water Absorption (%)	Bulk Density (kg/m^3)	Apparent Density (kg/m^3)	Moisture Content (%)	Silt Content (%)
Mixed coral sand	3.52	3.73	1296	2707	2.87	0.5

Table 3 presents the mix proportion for the CAGC. The binder included high-activity, alkaline S95-grade slag powder, and Class I fly ash. The alkaline activator was a sodium silicate solution with a modulus of 1.0, and seawater was prepared according to the artificial seawater formulation by Liu [35], with the main components shown in Table 4 and Composition shown in Table 5. The slag powder (SL) was a high-activity, alkaline S95-grade slag powder. The fly ash (FA) was Class I fly ash. The alkaline activator was prepared by mixing liquid sodium silicate and solid NaOH particles, with sodium silicate having a modulus of 2.46, and sodium silicate containing 12.40% Na_2O and 29.54% SiO_2. Additionally, the NaOH used had a purity of 99% or higher. The combination of these materials adjusted the sodium silicate modulus to 1.0. To improve the workability of the concrete, a QS-8020 polycarboxylate superplasticizer (PS) (Shanghai Qinhe Chemical Products Co., LTD) was used. Uniaxial compression tests were conducted on cubic specimens (150 × 150 × 150 mm) and prism specimens (150 × 150 × 300 mm) under the same curing conditions to obtain their compressive strength (f_{cu}), axial compressive strength (f_c), and uniaxial compressive stress–strain curves, where f_{cu} is the measured compressive strength of the concrete cube for 28d curing; f_c is the measured value of the axial compressive strength of the concrete for 28d curing.

Table 3. Mixing proportion.

Coarse Aggregate (kg/m^3)	Fine Aggregate		SL (kg/m^3)	FA (kg/m^3)	Alkali Activator		Seawater (kg/m^3)	f_{cu} (MPa)	f_c (MPa)
	Coarse Sand (kg/m^3)	Fine Sand (kg/m^3)			Sodium Silicate (kg/m^3)	NaOH Solution (kg/m^3)			
711	336	336	167	250	142	127	60	37.6	29.0

Table 4. Main compound composition of artificial seawater.

No.	NaCl	$MgCl_2 \bullet 6H_2O$	Na_2SO_4	$CaCl_2$
Content/(g/L)	28.1	7.22	2.43	1.12

Table 5. Composition and proportion of SL and FA.

No.	Ingredient Composition							
	Al_2O_3 (%)	SiO_2 (%)	Fe_2O_3 (%)	CaO (%)	MnO (%)	MgO (%)	K_2O (%)	Na_2O (%)
SL	14.3	36.5	3.2	33.6	0.8	7.5	\	\
FA	28.1	50.8	6.2	3.7	1.2	28.1	0.6	1.2

2.2. Tensile Performance of SSRs

Figure 6 shows the 304 SSR used in this study. According to the standard GB/T228.1-2021 [36], a WAW-600 electro-hydraulic servo testing machine (Yanrun Light Machine Technology Co., Ltd. in Shanghai, China)was employed to conduct tensile tests on SSRs of various diameters at room temperature (Figure 7). Table 6 shows the fundamental mechanical properties of the SSRs. Unlike an ordinary carbon steel rebar, the SSR did not exhibit a yield plateau; therefore, its nominal yield strength was defined as the stress corresponding to a 0.2% plastic strain. The nominal yield strength of the SSR was 515.0 MPa, with a tensile strength of 804.1 MPa, an average elastic modulus of 167.1 GPa, and an elongation after fracture of 40.0%, indicating it was a ductile rebar material.

Figure 6. SSRs.

Figure 7. Tensile test of SSRs.

Table 6. Mechanical properties of SSRs.

d (mm)	Nominal Yield Stress $R_{P0.2}$ (MPa)	Ultimate Stress R_m (MPa)	Modulus of Elasticity E_s (GPa)
8	511.1	799.1	165.1
12	515.4	807.5	167.2
16	516.8	806.6	166.8
20	516.7	803.3	169.1

2.3. Eccentric Compression Column Design

Table 7 shows the detailed parameters of each specimen, where b is the width, h is the height, and l is the length of the cross-section of the SCGCs, in mm; d is the diameter of the longitudinal bars, in mm. Figure 8 shows the schematic diagram of the distribution of reinforcement bars in the specimens, where "D^{SS}" represents the 304 SSR used in this test. The longitudinal and transverse reinforcement of the eight SCGC specimens used 304 SSRs, labeled as SCGC1 to SCGC8, according to different values of ρ_s and e_0. The specimens had a rectangular cross-section with dimensions of 250 mm × 300 mm and a symmetrical reinforcement arrangement. The central section included four longitudinal SSRs of the same diameter, with the longitudinal reinforcement ratios set at 0.302%, 0.536%, and 0.838%, and eccentricities set at 70 mm, 140 mm, 210 mm, and 280 mm. The stirrup diameter spacing was set at 200 mm, with a cover thickness of 30 mm, to closely match practical engineering conditions. Loading and end damage prevention were prioritized during testing. The ends of the SCGC specimens were equipped with enlarged loading flanges and densified stirrups in the flange area. The stirrup spacing was set at 100 mm. Additionally, two SSRs of the same diameter were added to increase the reinforcement ratio.

Table 7. Design parameters of SCGCs.

No.	Strength Grade	Size ($b \times h \times l$) (mm)	e_0 (mm)	d (mm)	ρ_s (mm)	Stirrup (mm)
SCGC1	C30	250 × 300 × 1600	70	12	0.302	8@200
SCGC2	C30	250 × 300 × 1600	280	12	0.302	8@200
SCGC3	C30	250 × 300 × 1600	70	16	0.536	8@200
SCGC4	C30	250 × 300 × 1600	140	16	0.536	8@200
SCGC5	C30	250 × 300 × 1600	210	16	0.536	8@200
SCGC6	C30	250 × 300 × 1600	280	16	0.536	8@200
SCGC7	C30	250 × 300 × 1600	70	20	0.838	8@200
SCGC8	C30	250 × 300 × 1600	280	20	0.838	8@200

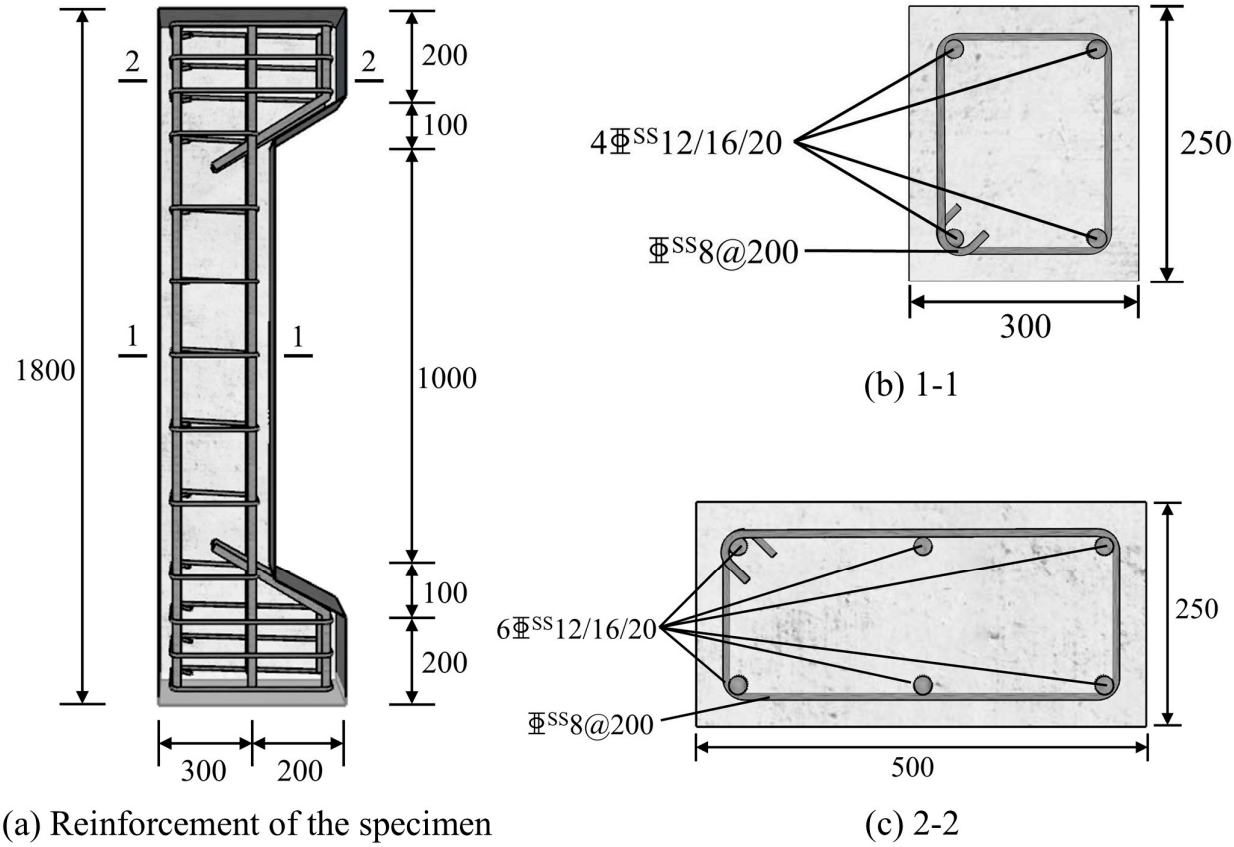

Figure 8. SCGC's basic size and reinforcement.

2.4. Test Setup

The tests were conducted using a YE-1000F electro-hydraulic servo press (Bonwei Electromechanical Control Engineering Co., Ltd. in Hangzhou, China) with a maximum load capacity of 10,000 kN (Figure 9a). To simulate the realistic stress state of eccentrically compressed members, a hinged support structure composed of rollers and loading plates was installed at both ends of the specimen. Both rollers and loading plates were fabricated from Q235 steel, with their long sides matching the width of the specimen's cross-section (Figure 9b). Pre-marked load application points on the top and bottom surfaces of the specimen enabled the adjustment of the hinged support positions, thereby facilitating the application of various eccentric loads. Strain and displacement data at each loading stage were recorded using a DH3821 static strain measurement system (Donghua Test Technology Co., Ltd. Jingjiang, China).

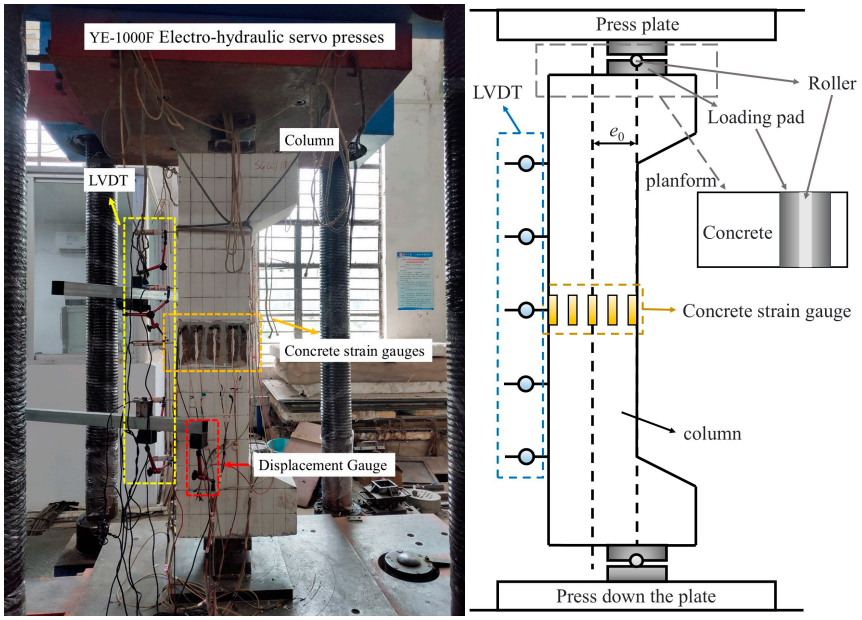

(**a**) (**b**)

Figure 9. Loading of specimen. (**a**) Column loading. (**b**) Load scheme.

Figure 10 shows the placement of lateral displacement meters, strain gauges on longitudinal reinforcement, and strain gauges on concrete. Displacement meters were evenly arranged along the height of the column to capture lateral displacements at different stages. Additionally, a single displacement meter was placed on the side to monitor whether the specimen was subjected to unidirectional eccentric compression during loading. A crack width detector was used to observe and measure crack widths, while a ruler was used to measure crack spacing. Concrete strain gauges were evenly attached at the mid-height of the column to measure longitudinal strain at various stages. Strain gauges were also attached at the mid-section of the longitudinal reinforcement and 200 mm above and below this point to measure the strain behavior of the SSR at each stage.

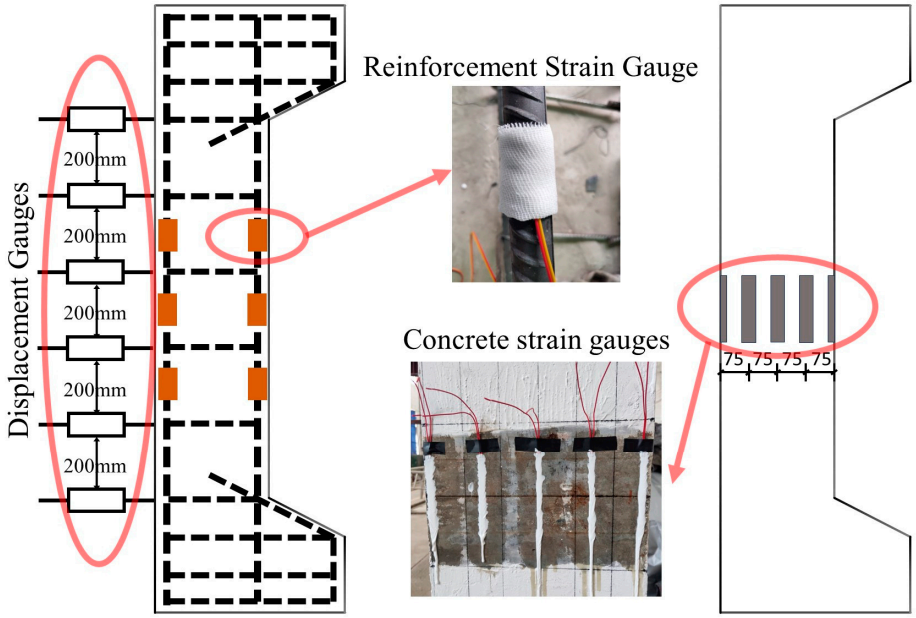

Figure 10. Arrangement of strain gauges and displacement gauges.

3. Test Result and Analysis

3.1. Failure Patterns and Crack Development

Figure 11 shows the failure patterns of the selected SCGC specimens (taking SCGC2, SCGC5, and SCGC6 for examples). Figure 12 shows the crack propagation in the SCGCs (taking SCGC2, SCGC5, and SCGC6 for examples). While the failure pattern of SCGCs under combined compression and bending is similar to the eccentric compression patterns observed in ORC columns by Li [22], the SCGCs exhibit greater lateral deformation.

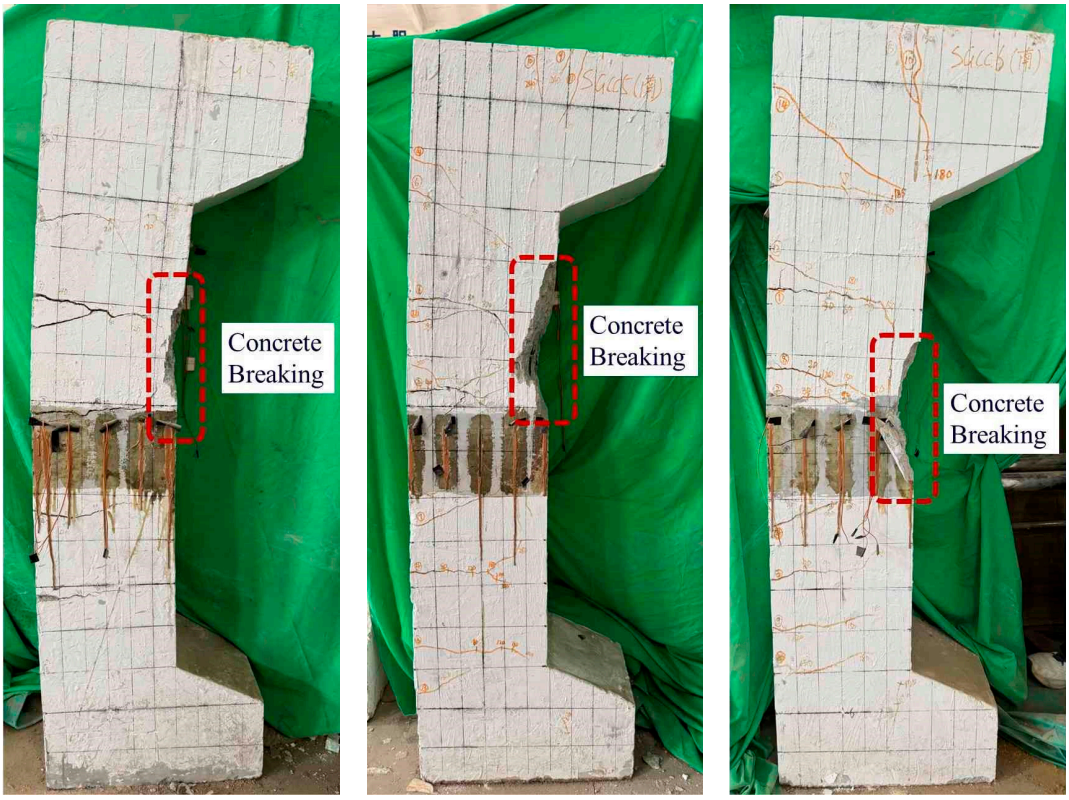

(**a**) SCGC2. (**b**) SCGC5. (**c**) SCGC6.

Figure 11. The failure patterns of typical SCGC specimens.

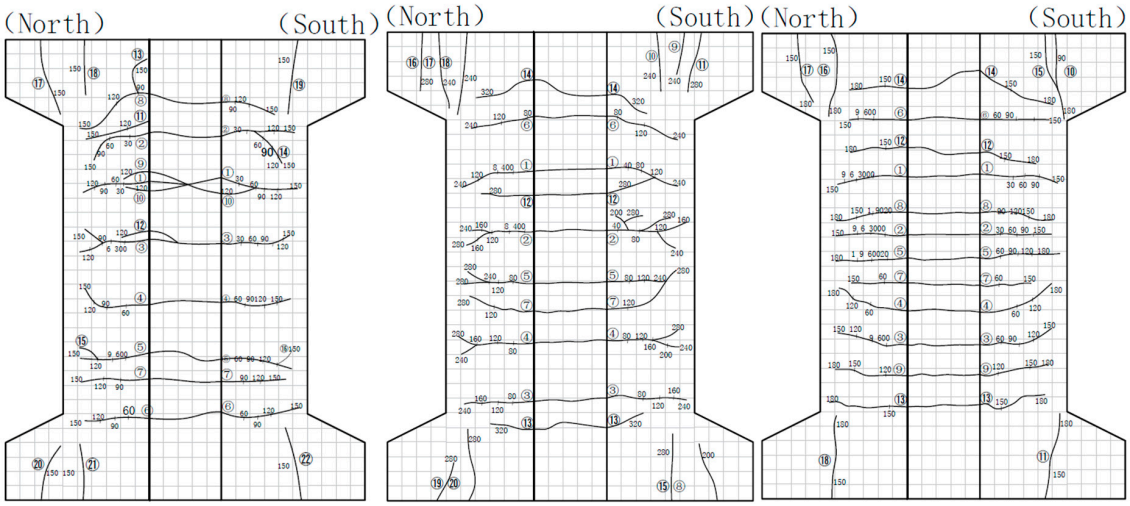

(**a**) SCGC2 (**b**) SCGC5 (**c**) SCGC6

Figure 12. Crack development diagram. Note: Numbers 1–22 in the figure show the chronological order of cracks.

When the external load reached 10% to 16% of the ultimate load capacity (N_u), the concrete in the tension zone of the eccentrically loaded columns began to crack, initiating the first horizontal crack. When the load reached 18% to 25% of N_u, a second horizontal crack appeared in the tension zone, and in some cases, a third crack was observed. At 30% to 70% of N_u, the cracks formed in the earlier stages continued to propagate toward the compression zone, while additional fine cracks emerged in the tension zone and progressively widened. When the load reached 70% to 82% of N_u, the number of cracks stabilized, and longitudinal cracks began to form at the supports and in the compression zone. When the ultimate load was reached, the concrete in the compression zone suddenly crushed, signaling the failure of the specimen. The total number of cracks ranged between 16 and 22.

Figures 13 and 14 present the experimental results of the cracking load (N_{cr}) and ultimate load (N_u) of the SCGC. As the eccentricity increased, both N_{cr} and N_u of the SCGC decreased; with the increase in the reinforcement ratio, N_u increased, but N_{cr} showed no significant change. For the SCGC with the same ρ_s, when e_0 was increased to 2, 3, and 4 times its initial value of 70 mm, N_{cr} decreased by 25%, 67%, and 75%, respectively, while N_u decreased by 40%, 71%, and 80%. For the SCGC with the same e_0, when ρ_s was increased by 1.77 times and 2.77 times from the initial 0.302%, N_u increased by 12.6% and 27.2%, respectively. However, before the SCGC cracked, the strain in the SSR was minimal, resulting in negligible tensile stress. Therefore, the tensile resistance of the SCGC was primarily provided by the concrete, making the influence of ρ_s on N_{cr} insignificant.

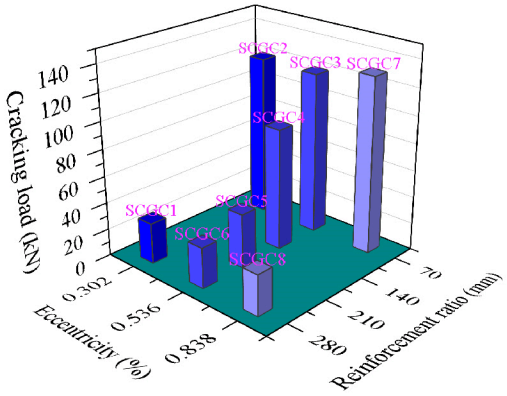

Figure 13. Cracking load.

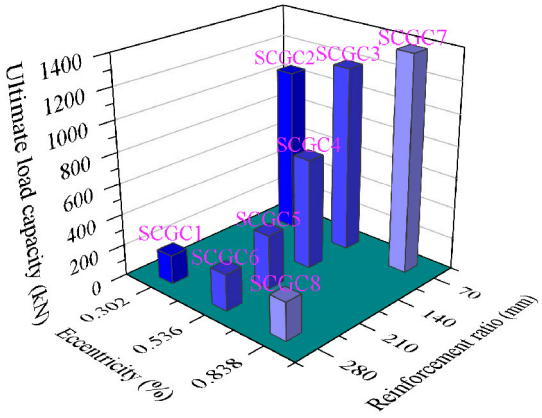

Figure 14. Ultimate load.

Figure 15 shows the relationship between $N/f_c bh$ and the crack width. It can be observed that an increase in e_0 or a decrease in ρ_s accelerates the rate of crack width development, and the crack width development for each SCGC shows an approximately linear trend.

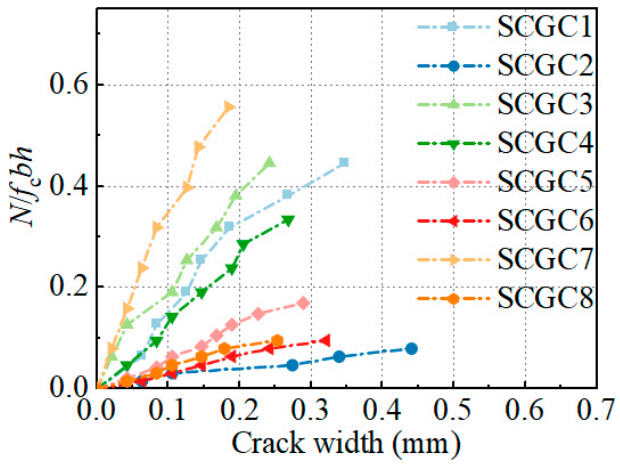

Figure 15. N/f_cbh—crack width curves.

3.2. Deformation Analysis

Figure 16 shows the effect of e_0 and ρ_s on the load–axial displacement curves. While the overall trends of these curves are similar, there are notable differences. The axial deformation of the specimens consists of two components: the axial compression deformation of the specimens themselves and the axial displacement due to bending. The latter is the dominant factor. The curves show an almost linear relationship in the early and middle stages of loading. However, the curves start to smooth out in the later stages, especially near the peak load. The curves become progressively smoother as e_0 increases (or ρ_s decreases), indicating an increase in ductility.

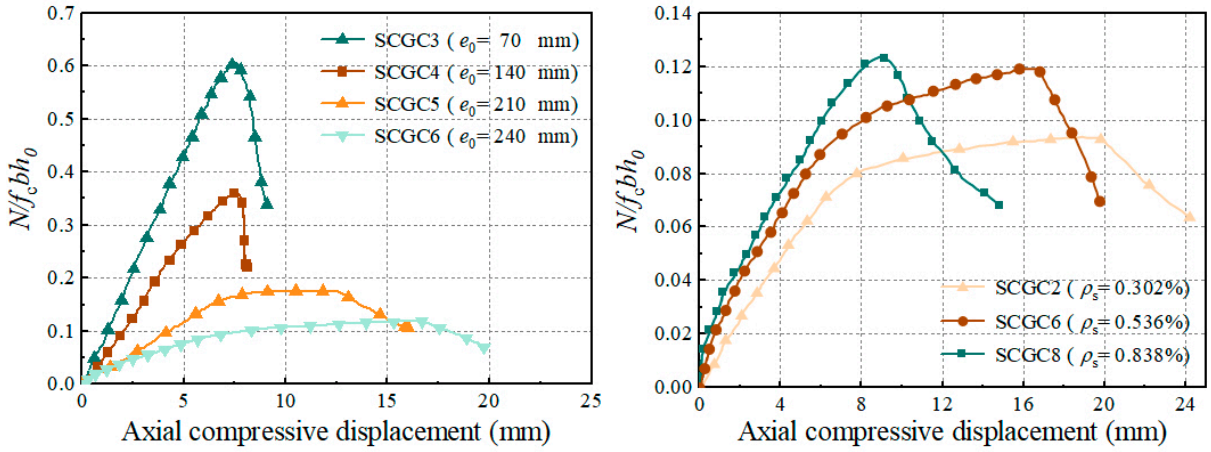

(**a**) Eccentricity. (**b**) Reinforcement ratio.

Figure 16. N/f_cbh_0—axial compressive displacement curves.

Figure 17 illustrate the effects of e_0 and ρ_s on the load–midspan lateral displacement curves. The overall trends of these curves are consistent. Cracks on the tension side of the column appear earlier in the early stage of loading, as e_0 increases (or ρ_s decreases). This leads to a significant reduction in the lateral stiffness. Consequently, there is a marked increase in the midspan lateral deflection. The lateral displacement curves of the column become steeper as e_0 increases (or ρ_s decreases) during the mid-to-late stages of loading.

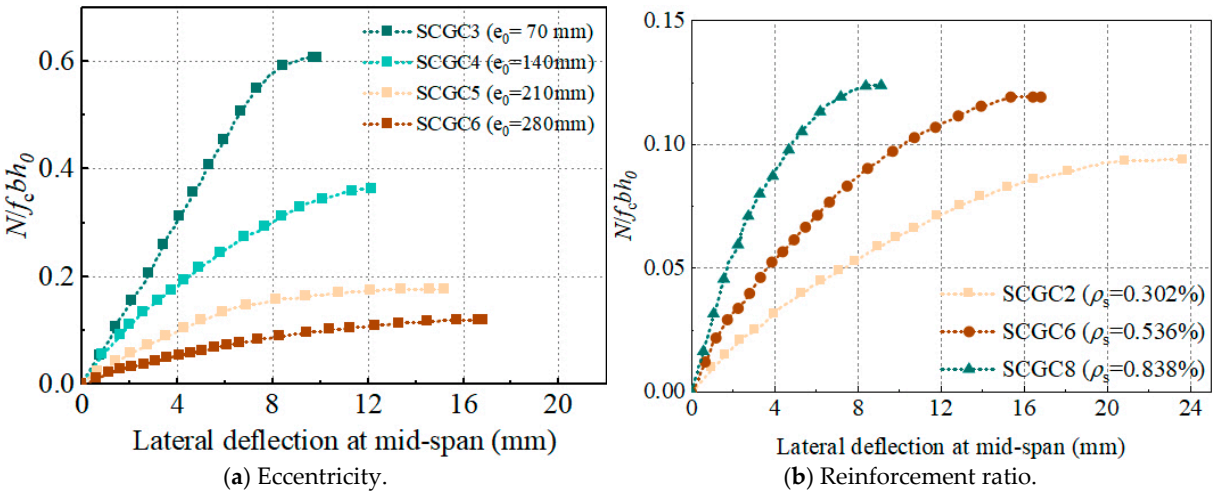

(**a**) Eccentricity. (**b**) Reinforcement ratio.

Figure 17. N/f_cbh_0—midspan lateral displacement curve.

Figure 18 presents the lateral displacement curves of SCGC2, SCGC5, and SCGC6 under various loading stages. It can be observed from Figure 18 that the lateral displacement curves exhibit a half-sine wave distribution form from the initial loading of the SCGC until the failure stage. The shape conforms to the function of a standard sine curve, expressed as $f_1 = f\sin(\pi x/l)$, where f_1 is the lateral deflection, in mm; f is the maximum midspan lateral deflection under each load stage, in mm; and l is the height of the column, in mm.

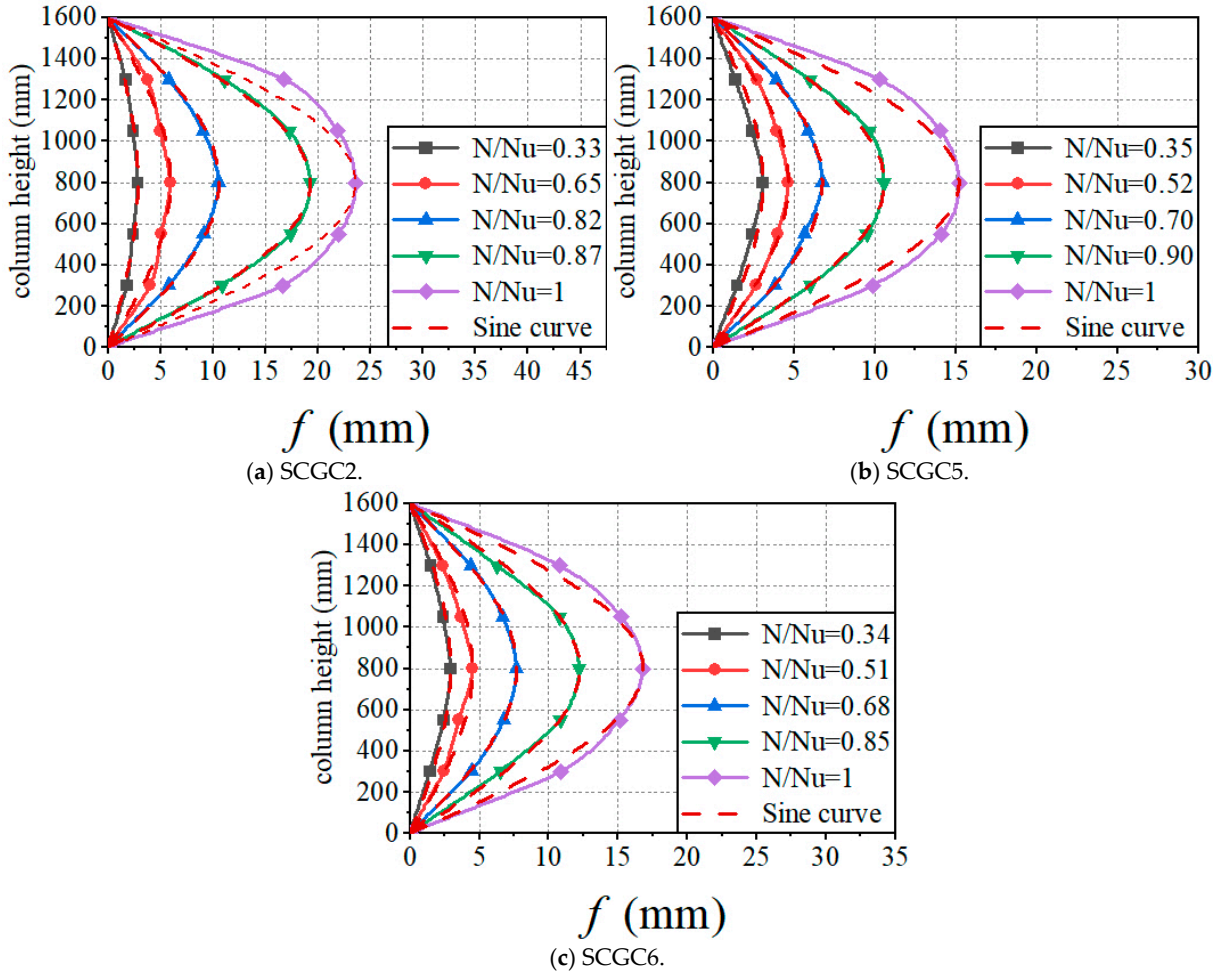

(**a**) SCGC2. (**b**) SCGC5.

(**c**) SCGC6.

Figure 18. Deflection distribution in the direction of sample height.

3.3. Strain Analysis

Figure 19 shows the $N/f_c bh$—SSR strain relationship curves (taking SCGC2, SCGC5, and SCGC6 for examples). In these curves, "CR" represents the compressive SSR, "TR" represents the tensile SSR, and ε_{sy} represents the tensile yield strain of the SSR. It can be observed that under large eccentricity ($e_0/h \geq 0.7$), the SSR on the side farther from the axial force reaches its tensile yield strength, indicating full utilization. Additionally, the tensile and compressive curves of the SSR show different rising trends, exhibiting distinct tension–compression behavior, which is consistent with the findings of Yuan [19].

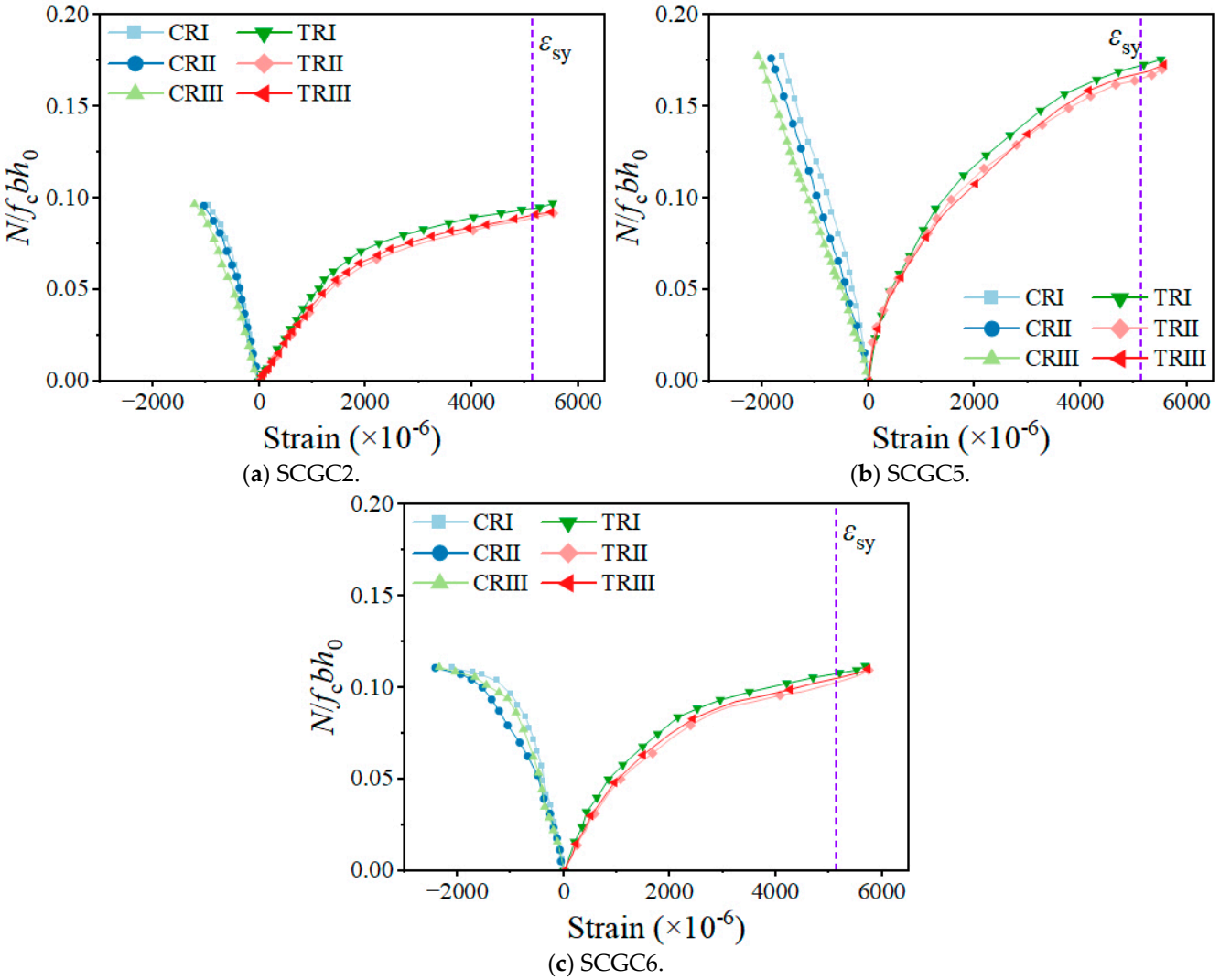

(**a**) SCGC2. (**b**) SCGC5.

(**c**) SCGC6.

Figure 19. $N/f_c bh$—SSR strain relationship curves.

Figure 20 shows the concrete strain distribution at the midspan section during various loading stages (taking SCGC1, SCGC4, and SCGC6 for examples). Here, ε_{sc} represents the SSR strain on the side closer to the axial force and ε_{st} represents the SSR strain on the side farther from the axial force. The average strain across the transverse section of the SCGC is almost linearly distributed. As the external load increases, the neutral axis gradually shifts toward the edge of the compressive zone of the SCGC. During loading, the concrete strain of the midspan section varies roughly linearly along the height of the section, consistent with the assumption of a planar section.

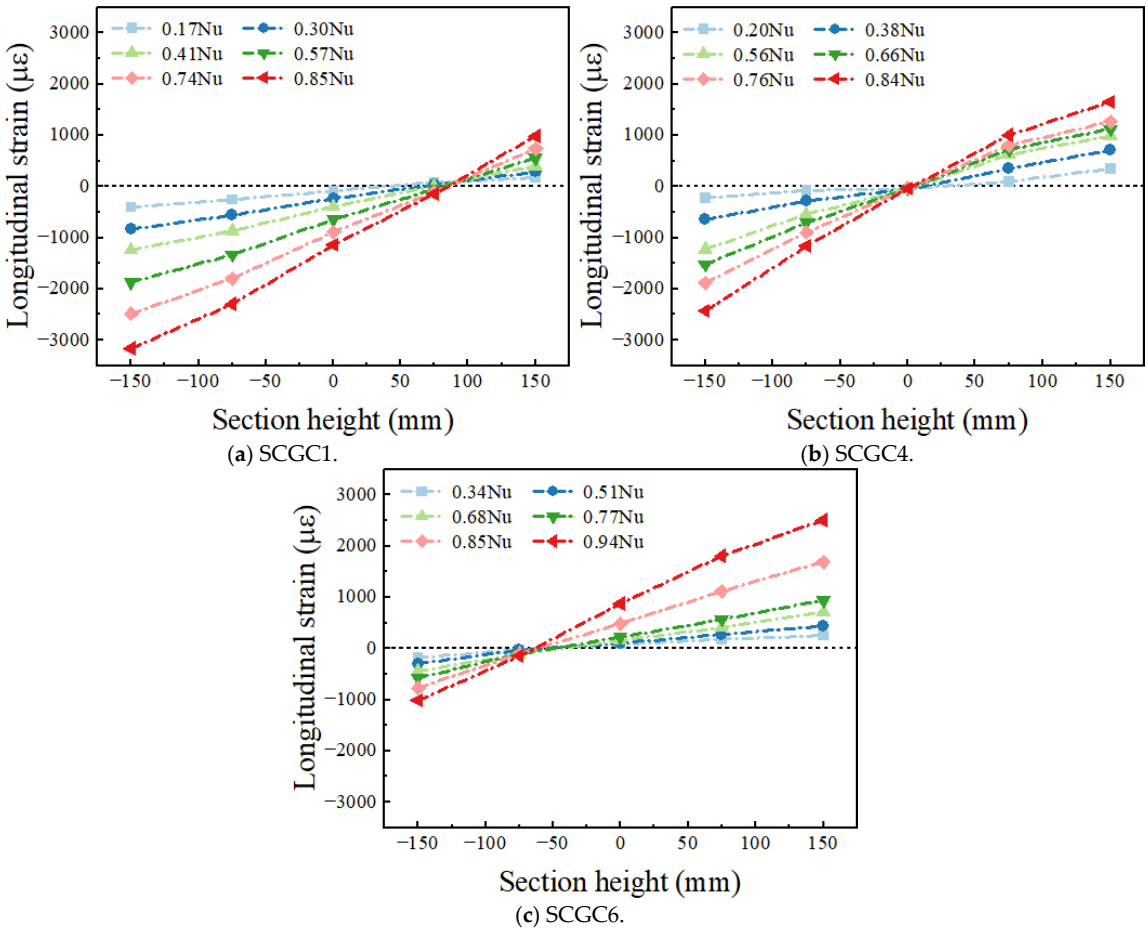

(**a**) SCGC1. (**b**) SCGC4.

(**c**) SCGC6.

Figure 20. Concrete strain distribution diagram of midspan section.

4. Analysis of the Bearing Capacity and Crack Width of SCGCs

4.1. Constitutive Relationship of CAGC

The uniaxial constitutive model comprehensively reflects the mechanical behavior of concrete under uniaxial loading and plays a crucial role in the design and analysis of reinforced concrete structures [37]. When investigating the uniaxial constitutive relationship of CAGC, the compressive results of prismatic specimens from Section 2.1 were compared with studies by Liu [38] and Da [39], as shown in Figure 21.

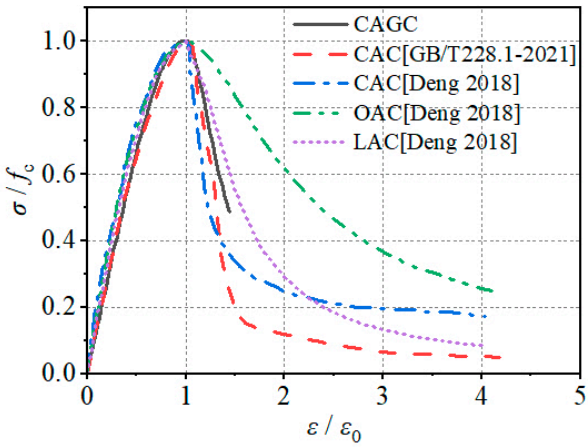

Figure 21. The stress–strain curves of CAGC, CAC, OAC, and LAC. Refs. [36,37].

It can be observed that in the ascending segment, the curves for CAC, ordinary aggregate concrete (OAC), and lightweight aggregate concrete (LAC) are almost identical to the CAGC curve. However, in the descending segment, the CAGC curve is steeper than the OAC and LAC, but flatter than the CAC. Overall, the constitutive relationship curve of CAGC significantly differs from that of CAC, OAC, and LAC, indicating that their stress–strain relationships are not applicable to CAGC.

Therefore, this paper proposes an optimized uniaxial constitutive model for CAC, based on the work of Liu [38] and Da [39], as shown in Equation (1). A fitting analysis was conducted, and the results are presented in Figure 22.

$$\frac{\sigma}{f_c} = \begin{cases} \left[a\left(\frac{\varepsilon}{\varepsilon_0}\right) + (3-2a)\cdot\left(\frac{\varepsilon}{\varepsilon_0}\right)^2 + (a-2)\cdot\left(\frac{\varepsilon}{\varepsilon_0}\right)^3\right] & 0 \le \varepsilon < \varepsilon_0 \\ \dfrac{\varepsilon/\varepsilon_0}{b(\varepsilon/\varepsilon_0 - 1)^2 + \varepsilon/\varepsilon_0} & \varepsilon_0 \le \varepsilon \le \varepsilon_{cu} \end{cases} \quad R^2 = 0.991 \tag{1}$$

where σ is the stress of CAGC, in MPa; f_c is the axial compressive strength of CAGC, with a measured value of f_c = 29.0 MPa in this study; ε is the strain of CAGC; ε_0 is the compressive strain of CAGC when the compressive stress reaches f_c, with ε_0 = 0.0024; ε_{cu} is the ultimate compressive strain of CAGC, taken as ε_{cu} = 0.0028; and a and b are the control parameters for the ascending and descending segments of the curve, with values of a = 1.31 and b = 7.892, respectively.

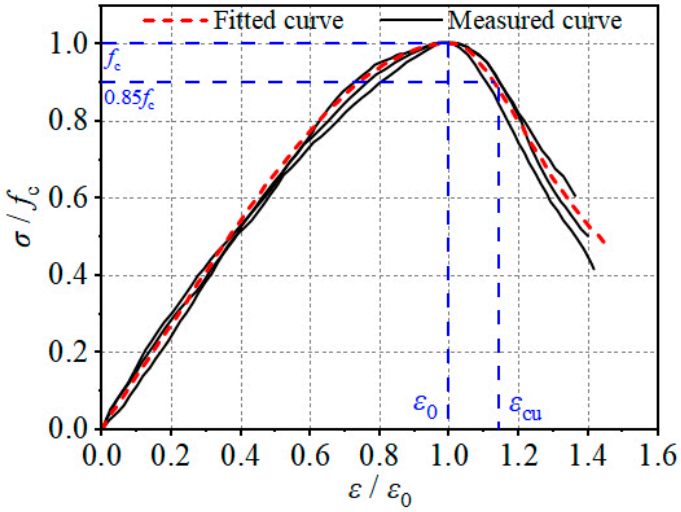

Figure 22. Normalized stress–strain curves.

This constitutive model is considered for practical engineering applications, with attention to the safety reserve requirements of the project. Notably, the stress in the ε_0 ~ ε_{cu} range does not significantly decrease. This paper adopts a horizontal line for the descending segment and truncates it at ε_{cu}, referring to the provisions of GB50010-2010 [40] on post-peak concrete behavior, as shown in Figure 23. The resulting uniaxial constitutive relationship expression for CAGC is:

$$\frac{\sigma}{f_c} = \begin{cases} \left[a\left(\frac{\varepsilon}{\varepsilon_0}\right) + (3-2a)\cdot\left(\frac{\varepsilon}{\varepsilon_0}\right)^2 + (a-2)\cdot\left(\frac{\varepsilon}{\varepsilon_0}\right)^3\right] & 0 \le \varepsilon < \varepsilon_0 \\ f_c & \varepsilon_0 \le \varepsilon \le \varepsilon_{cu} \end{cases} \tag{2}$$

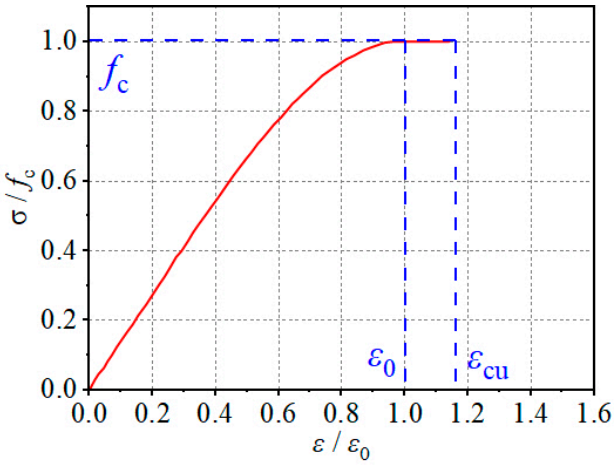

Figure 23. Compression stress–strain curve of CAGC.

4.2. Bearing Capacity

4.2.1. Calculation and Analysis of N_u

The calculation of N_u in this study is based on the following assumptions: (1) The SCGC satisfies the plane section assumption during loading (verified in Section 3.3); (2) The tensile strength of CAGC is not considered in the calculation; (3) The concrete stress in the compression zone of the SCGC section is calculated using an equivalent rectangular stress distribution; (4) With a slenderness ratio l/b = 1000/250 = 4, the test columns are considered short columns, and second-order effects are neglected in the calculation.

This paper establishes formulas for different failure patterns and load-bearing capacity based on these assumptions. As shown in Figure 24, the failure patterns of the SCGC are classified into large eccentric compression and small eccentric compression. In these formulas, e_i, e_t, and e_c represent the distances between the external load and the section center, the tensile SSR, and the compressive SSR, respectively; σ_s and σ_s' are the SSR stresses far from (A_s) and near (A_s') the external load; α_1 is the rectangular stress coefficient; x_c, x_b, and x denote the actual height of the CAGC in compression, the limiting height of the compression zone, and the calculated height, where $x = \beta_1 x_c$; ε_t and ε_y are the strains of the SSR far from the external load and its nominal yield strain, respectively; and ε_c and ε_{cu} are the strains of the SSR near the external load and at the section edge, respectively.

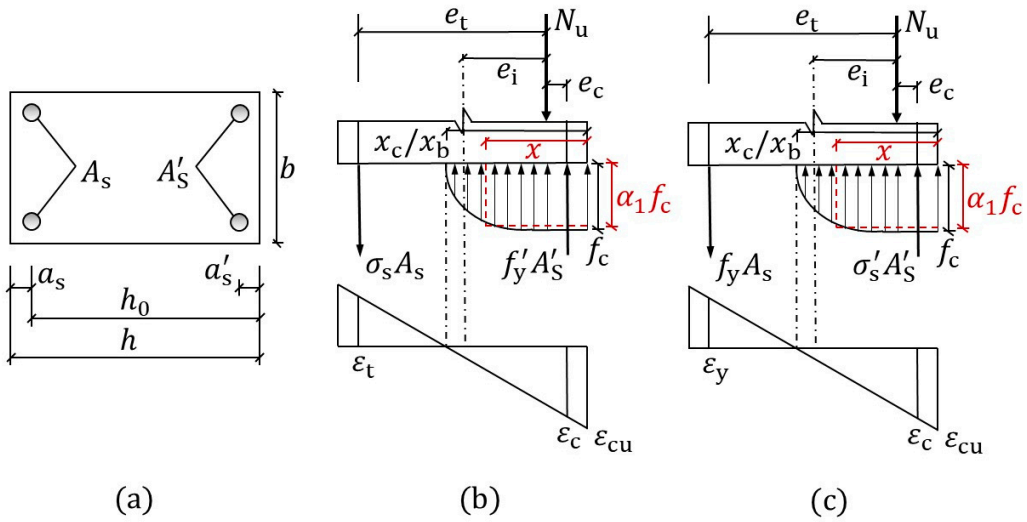

Figure 24. Force diagram of column section. (**a**) Column section (**b**) Large eccentric compression mode (**c**) Small eccentric compression mode.

When the external load acts on the SCGC with a small e_0, the SCGC section will experience a small eccentric compression, as shown in Figure 24b. At this time, the concrete in the compression zone reaches its compressive strength, and the steel reinforcement on the side farther from the axial force has not reached its yield state, whether it is in compression or tension. Therefore, based on the plane section assumption and force equilibrium, the following formula can be derived:

$$N_u e_t = \alpha_1 f_c b x (h_0 - x/2) + f'_y A'_s (h_0 - a'_s) \quad (3)$$

$$N_u = \alpha_1 f_c b x + f'_y A'_s - \sigma_s A_s \quad (4)$$

where f'_y is the design value of the compressive strength of the SSR, in MPa. When e_0 is large, the SCGC section will experience large eccentric compression, as shown in Figure 24b. The steel reinforcements that are farther from the axial force reach the yield state, and the concrete in the compression zone reaches its compressive strength. However, it is verified that the steel reinforcement that is closer to the axial force has not reached its yield state based on the strain measurements of the SSR. Therefore, based on the plane section assumption and force equilibrium, the following formula can be derived:

$$N_u e_t = \alpha_1 f_c b x (h_0 - x/2) + \sigma'_s A'_s (h_0 - a'_s) \quad (5)$$

$$N_u = \alpha_1 f_c b x + \sigma'_s A'_s - f_y A_s \quad (6)$$

where f_y is the design value of the compressive strength of the SSR, in MPa. Determining the compression state directly influences the force calculations, as observed from the analysis. Additionally, the relative boundary compression zone height ξ_b serves as a key criterion for distinguishing between large and small eccentric failures.

According to Equation (7), the boundary relative compression zone height is determined to be $\xi_b = 0.443$, which allows for the classification of the SCGC into large and small eccentric compression categories, as shown in Figure 25.

$$\xi_b = \frac{x_b}{h_0} = \frac{\beta_1 \varepsilon_{cu}}{\varepsilon_{cu} + \varepsilon_y} \quad (7)$$

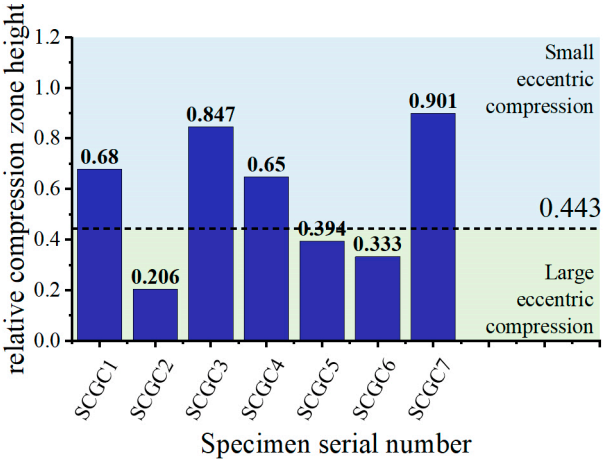

Figure 25. Relative depth of compressive area.

In summary, the SCGC specimens tested in this study do not exhibit full-section compression. SCGC8 experienced premature failure due to the slippage of the reinforcement in the anchorage region, resulting in significantly lower load-carrying capacity and thus is excluded from the load-carrying capacity analysis. When e_0 = 70 mm and 140 mm, the

specimens exhibit small eccentric compression failure; when e_0 = 210 mm and 280 mm, the specimens experience large eccentric compression failure.

4.2.2. Model Optimization

Considering that the coral aggregate is a lightweight aggregate, according to the "Code for Design of Lightweight Aggregate Concrete Structures" (JGJ12-2006) [41], the calculation formula for N_u of a rectangular column under combined axial and bending loads is as follows:

$$\begin{cases} N_u \le f_{cm} b x + f'_y A'_s - f_y A_s \\ N_u e \le f_{cm} b x (h_0 - x/2) + f'_y A'_s (h_0 - a'_s) \\ e = \eta e_i + h/2 - a_s \\ \eta = 1 + \frac{1}{1400(e_0/h_0)} \left(\frac{l_0}{h}\right)^2 \zeta_1 \zeta_2 \\ \zeta_1 = 0.5 f_c A / N \\ \zeta_2 = 1.3 - 0.015 l_0 / h \\ e_i = e_0 + e_a \\ e_a = 0.12(0.3 h_0 - e_0) \end{cases} \quad (8)$$

where f_y and f'_y are the tensile and compressive strengths of the reinforcement, in MPa, respectively; A_s and A'_s are the cross-sectional areas of the tensile and compressive longitudinal reinforcements, in mm^2, respectively; a_s and a'_s are the distances from the resultant force points of the tensile and compressive reinforcements to the edge of the cross-section, in mm, respectively; e is the distance between the point of axial load and the resultant force point of the tensile reinforcement, in mm, respectively; e_i is the initial eccentricity, in mm; e_0 is the eccentricity of the axial load relative to the centroid of the cross-section, in mm; e_a is the additional eccentricity, in mm; f_{cm} is the bending compressive strength of the concrete, in MPa, where f_{cm} = 1.05f_{cu}; η is the moment increase factor due to second-order effects; l_0 is the effective length of the member, in mm; and ζ_1 and ζ_2 are fitting parameters, where ζ_2 = 1 when l l_0/h < 20.

The ultimate bearing capacity (N_u) of seven SCGC specimens under eccentric loading was calculated based on the JGJ12-2006. The average ratio of the calculated values ($N_u{}^c$) to the measured values (N_u) is 3.07, with a coefficient of variation of 0.58. As shown in Figure 26, the bearing capacity calculated according to the JGJ12-2006 is generally overestimated, leading to poor prediction results. The main reasons are as follows: (i) CAGC is the combination of a geopolymer and coral aggregate, whose mechanical properties differ significantly from those of GPC and lightweight aggregate concrete; (ii) The plastic properties of the SSR result in greater deformation and wider cracks in SSRC structures during normal service, and its high ductility leads to different load redistribution and stress redistribution patterns compared to ORC structures. Additionally, the asymmetry in the stress–strain curve of the SSR under tensile and compressive loads also contributes to the inapplicability of the existing bearing capacity calculation formulas.

In order to cope with the problems above, Equation (8) is modified in this paper.

On the one hand, the differences in equivalent stress calculations are caused by the distinct mechanical properties between the CAGC and LAC. This paper determines the equivalent rectangular stress block for the compression zone of the SCGC based on ensuring that the area of the equivalent rectangular stress block equals the area of the theoretical stress block, and keeping the position of the resultant force unchanged.

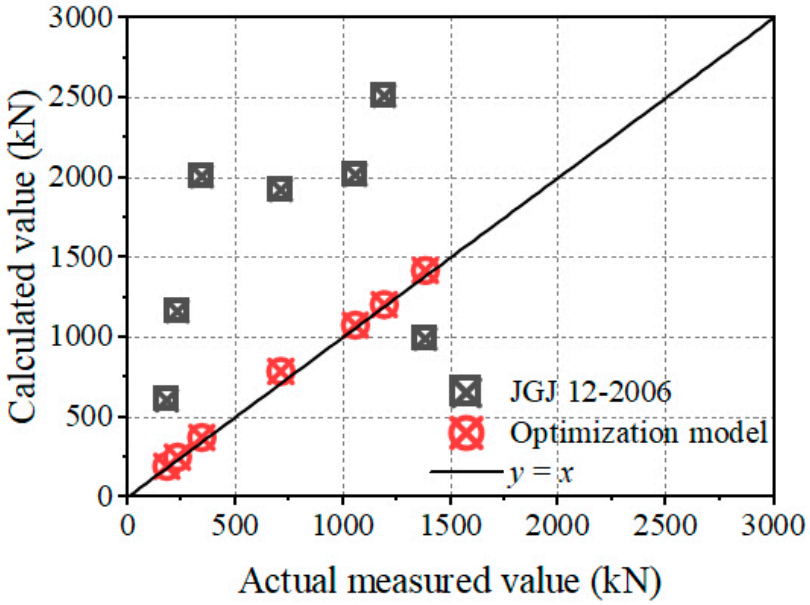

Figure 26. N_u^S vs. N_u.

In the equivalent stress diagram (Figure 27), x represents the equivalent length (shaded area in Figure 27). And OA corresponds to the parabolic portion of the theoretical stress block, while AB represents the rectangular portion of the theoretical stress block:

$$OA = \frac{\varepsilon_0}{\varepsilon_{cu}} x = \frac{0.0024}{0.0028} x = \frac{6}{7} x \tag{9}$$

$$AB = \left(1 - \frac{\varepsilon_0}{\varepsilon_{cu}}\right) x = \frac{1}{7} x \tag{10}$$

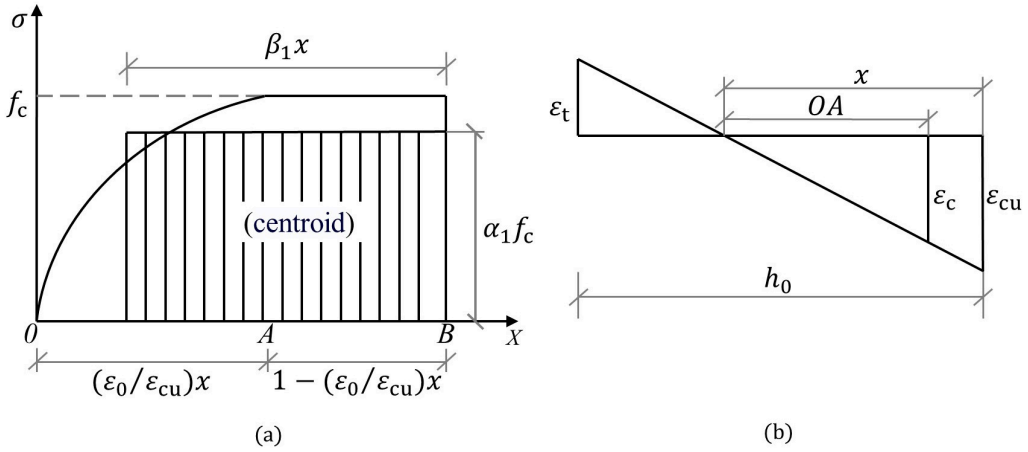

Figure 27. Equivalent stress. (**a**) Equivalent compressive stress of concrete (**b**) Strain distribution of column section.

The resultant compressive force D of the concrete can be determined from the area of the theoretical stress block:

$$D = D_1 + D_2 = \frac{2}{3} f_c \frac{24}{28} xb + f_c \frac{4}{28} xb = 0.714 xb \tag{11}$$

According to the method of calculating the static moment of area, the distance from the resultant compressive force point of the concrete to the compression edge of the section can be determined:

$$\frac{1}{2}\beta_1 x = \frac{f_c b\left(\frac{2}{3}\cdot\frac{24}{28}x\right)\left(\frac{4}{28}x+\frac{3}{8}\cdot\frac{24}{28}x\right)+f_c b\frac{4}{28}\left(\frac{1}{2}\cdot\frac{4}{28}x\right)}{0.714xb} = 0.38x \tag{12}$$

The value of β_1 is determined to be 0.76. The resultant compressive force D in the concrete, based on the area of the equivalent rectangular stress distribution, can be calculated as:

$$D = \alpha_1 f_c \beta_1 xb = 0.76\alpha_1 \sigma_0 xb \tag{13}$$

Equation (14) can be obtained from the equivalence principle.

$$0.76\alpha_1 f_c xb = 0.714 f_c xb \tag{14}$$

Hence, the value of α_1 is determined to be 0.94. For subsequent calculations, α_1 is taken as 0.94, and β_1 is taken as 0.76.

On the other hand, as discussed in Section 3.3, only the SSR that is farther from the axial force reaches the yield point under the large eccentricity failure pattern of the SCGC. This differs from the assumption in the JGJ12-2006 [41] code, which states that both the tensile and compressive reinforcements yield. However, the mechanical behavior of the SSR is similar to that described in the JGJ12-2006 [41] code under the small eccentricity failure pattern of the SCGC.

This paper derived Equations (15) and (16) based on the plane section assumption and force equilibrium to address this issue, in conjunction with Figure 27. The bearing capacity problem of large and small eccentric compression columns was resolved by solving these equations simultaneously with Equations (5) and (6).

$$\frac{\varepsilon_t}{\varepsilon_{cu}} = \frac{h_0 - x_c}{x_c} \rightarrow \varepsilon_t = \varepsilon_{cu}\left(\frac{h_0}{x_c} - 1\right) \tag{15}$$

$$\frac{\varepsilon_c}{\varepsilon_y} = \frac{x_c - a'_s}{h_0 - x_c} \rightarrow \varepsilon_c = \varepsilon_y\left(\frac{x_c - a'_s}{h_0 - x_c}\right) \tag{16}$$

This paper utilized the JGJ12-2006 [41] code in conjunction with the modified Ramberg–Osgood model to calculate the bearing capacity ($N_u{}^S$) of specimens SCGC1 to SCGC7, based on the aforementioned model revisions. The average ratio of $N_u{}^S$ to the measured bearing capacity N_u was found to be 0.94, with a coefficient of variation of 0.034. The calculation results are shown in Figure 26. In summary, the revised bearing capacity calculation model, combined with the modified Ramberg–Osgood model, provides a reliable prediction of the bearing capacity of SCGC.

4.3. Crack Width

Structural components must not only meet the relevant requirements for bearing capacity but also control cracks and deformations during their service life. According to the JGJ12-2006 [41], the calculation formula for the maximum crack width (ω_{max}) of rectangular columns under combined compression and bending is as follows:

$$\omega_{max} = \alpha_{cr}\psi\frac{\sigma_s}{E_s}\left(1.9C + 0.04\frac{d_{eq}}{\rho_{te}}\right) \tag{17}$$

where α_{cr} is the structural characteristic coefficient; ψ is the non-uniformity coefficient, $\psi = 1.1 - 0.65 f_t/\rho_{te}\sigma_s$; σ_s is the tensile stress of the SSR, in MPa; E_s is the elastic modulus of the steel, in GPa; C is the concrete cover thickness, in mm; ρ_{te} is the ratio of the SSR cross-sectional area A_f to the effective tensile area of the concrete A_{te}, $\rho_{te} = A_f/A_{te}$, where $A_{te} = 0.5bh$, h and b are the height and width of the cross-section, respectively; and d_{eq} is the equivalent diameter of the longitudinal tensile reinforcement, in mm, $d_{eq} = \sum n_i d_i^2 / \sum n_i \upsilon_i d_i$, where d_i, n_i, and v_i are the nominal diameter (mm), number of bars, and relative bond characteristic coefficient of the i-th type of longitudinal tensile reinforcement, respectively.

As shown in Figure 28 (taking SCGC1, SCGC3, SCGC4, and SCGC7 for examples), the calculation formulas proposed by the aforementioned three standards fail to accurately describe the $N/f_c bh$–crack width curve. Considering the following factors: (i) the bond performance between the CAGC and SSR differs from that between OPC and carbon steel bars, so the ψ calculation formula has been revised as shown in Equation (18); (ii) under a small eccentric load, the tensile SSR strain $\varepsilon_s = \varepsilon_{cu}(h_0/x_c - 1)$, while under a large eccentric load, the tensile SSR strain $\varepsilon_s = \varepsilon_y$. In summary, the revised crack width calculation formula is shown below.

$$\begin{cases} \omega_{max} = \alpha_{cr}\psi\varepsilon_s\left(1.9C + 0.04\dfrac{d_{eq}}{\rho_{te}}\right) \\ \psi = 1.65 - 0.975 f_t/\rho_{te}\sigma_s \end{cases} \tag{18}$$

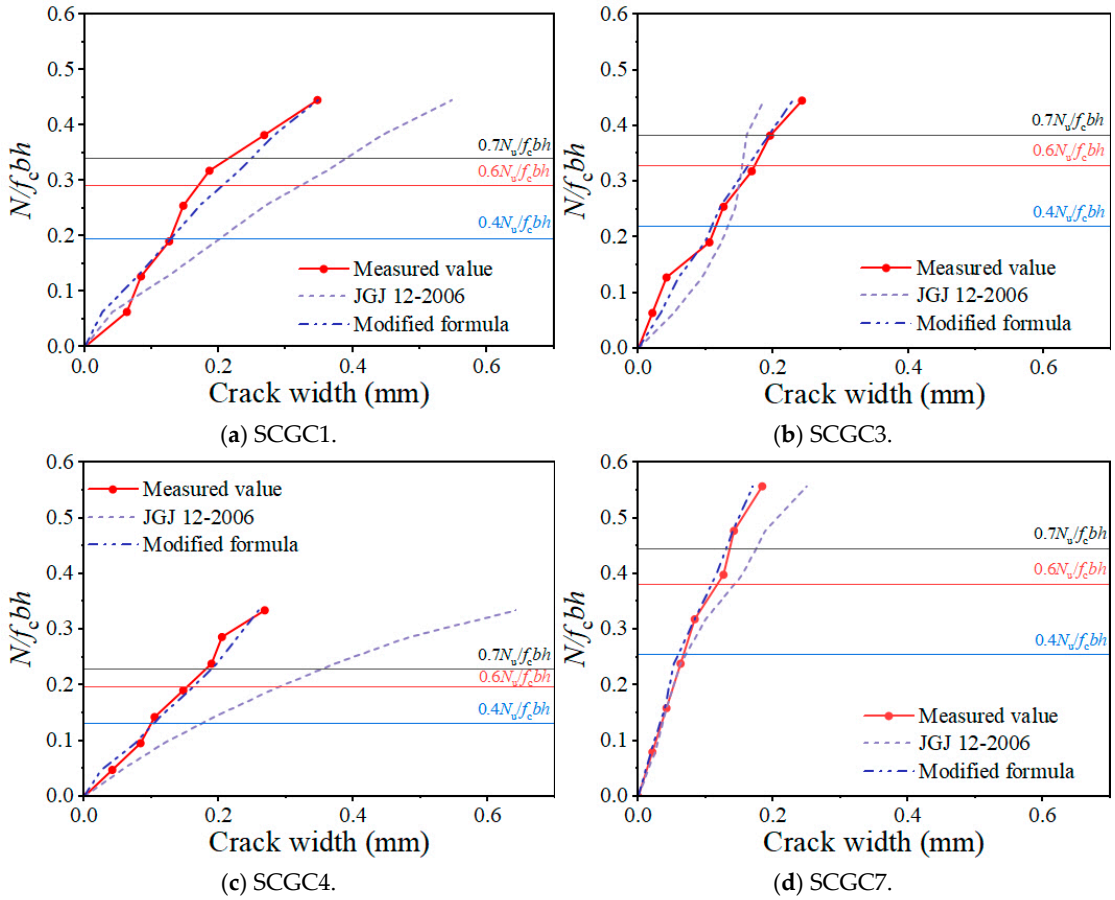

(**a**) SCGC1. (**b**) SCGC3.

(**c**) SCGC4. (**d**) SCGC7.

Figure 28. Comparison of test and predicted $N/f_c bh$—crack width curves.

Columns, which in actual engineering practice, are typically subjected to standard combination and quasi-permanent combination loads according to the GB50068-2018 [42]. The load factor γ is 1.367 for the standard combination. The relationship between the axial force N_k under the standard combination and the axial force design value N

is $N_k = N/1.367 = 0.7N$. Similarly, the load factor γ is 1.64 for the quasi-permanent combination. The relationship between N_k under the quasi-permanent combination and N is $N_k = N/1.64 = 0.6N$. Therefore, the standard combination and quasi-permanent combination loads correspond to 70% and 60% of the ultimate load, respectively. As shown in Figure 28, Equation (18) not only accurately predicts the crack width under standard combination (70% N_u) and quasi-permanent combination (60% N_u) loads but also effectively captures the overall trend of the $N/f_c bh$—crack width curve.

This paper proposes a column structure using a novel material—SCGC—that demonstrates the potential for practical application in island and marine buildings. The use of coral aggregates reduces material transportation costs and carbon emissions, while SSRs can help the structure face the durability challenges posed by the marine environmental context and extend the service life of marine structures. Therefore, this paper suggests the use of SCGC in the marine area with more coral waste. The failure mode of SCGC is similar to that of traditional concrete columns, but the mechanical properties of CAGC are different from ordinary concrete, and the SSR does not have a yielding platform, which leads to the existence of a special column stress situation and crack development, so this paper suggests the use of SCGC in real projects. The load carrying capacity prediction can be referred to Equations (5) and (6) and the crack width prediction can refer to Equation (18). The accuracy of these equations is verified in this paper and the results show that the equations are reliable.

5. Conclusions

This paper presents experimental and theoretical analyses of the eccentric compression of SCGC with different reinforcement ratios and eccentricity, leading to the following key conclusions:

(1) The failure patterns of SCGC under eccentric compression are similar to those of ORC columns, and its lateral displacement curve resembles a sine wave. However, SCGC exhibits greater lateral deformation compared to ORC.

(2) CAC, OAC, LAC, and CAGC exhibit a similar ascending branch. However, in the descending branch, the CAGC curve is steeper than that of the OAC and LAC curves, while flatter than that of the CAC curve. Through a systematic analysis of the stress–strain response characteristics specific to CAGC, this paper proposes a novel constitutive model for CAGC.

(3) When $e_0/h \geq 0.7$, SCGC experiences large eccentric failure; otherwise, it undergoes small eccentric failure. Under large eccentric compression, the tensioned SSR yields while the compressed SSR does not, which differs from that of reinforced OAC columns. Conversely, under small eccentric compression, the yielding behavior of the SSR is exactly opposite.

(4) This study proposes a novel load-bearing capacity prediction model for SCGC columns through the introduction of the CAGC constitutive model. The refined model demonstrates a strong agreement with the experimental results, indicating that it has promising applications.

(5) An improved crack width calculation model based on the bond-slip theory is developed, taking into account the different bonding characteristics between CAGC and SSR compared to OAC and carbon steel bars and the characteristic of SSRs lacking a yield plateau. The modified model is able to predict the crack width accurately.

Author Contributions: H.X.: Methodology, Visualization, and Supervision. J.J.: Writing—original draft and Formal analysis. C.Y.: Investigation. All authors have read and agreed to the published version of the manuscript.

Funding: This research received no external funding.

Institutional Review Board Statement: Not applicable.

Informed Consent Statement: Not applicable.

Data Availability Statement: The raw data supporting the conclusions of this article will be made available by the authors on request.

Conflicts of Interest: The authors declare that they have no known competing financial interests or personal relationships that could have appeared to influence the work reported in this paper.

References

1. Ebead, U.; Lau, D.; Lollini, F.; Nanni, A.; Suraneni, P.; Yu, T. A review of recent advances in the science and technology of seawater-mixed concrete. *Cem. Concr. Res.* **2022**, *152*, 106666. [CrossRef]
2. Da, B.; Yu, H.; Ma, H.; Tan, Y.; Mi, R.; Dou, X. Experimental investigation of whole stress-strain curves of coral concrete. *Constr. Build. Mater.* **2016**, *122*, 81–89. [CrossRef]
3. Yang, H.; Li, M.; Jiang, J.; Zhang, Y.; Mei, J.; Deng, Z. Mechanical properties of steel reinforced coral aggregate concrete column under uniaxial compression. *Constr. Build. Mater.* **2023**, *369*, 130508. [CrossRef]
4. Liang, X.; Yin, S.; Hu, C. Environmental reduction factors of BFRP bars in coral aggregate concrete in high temperature and high humidity environments. *Structures* **2021**, *33*, 3017–3024. [CrossRef]
5. Zi, M.; Liu, K.; Liu, S.; Qin, M. Study on the basic properties of coral sand used as fine aggregate. *Constr. Build. Mater.* **2015**, *5*, 11–14.
6. Zhao, Y.; Han, C.; Zhang, S.; Ge, R. Experimental study on the compression age strength of seawater coral concrete. *Concrete* **2011**, *2*, 43–45. (In Chinese)
7. Liu, J.; Ou, Z.; Mo, J.; Chen, Y.; Guo, T.; Deng, W. Effectiveness of saturated coral aggregate and shrinkage reducing admixture on the autogenous shrinkage of ultrahigh performance concrete. *Adv. Mater. Sci. Eng.* **2017**, *2017*, 2703264. [CrossRef]
8. Yang, H.; Mei, J.; Yang, Y. Bond strength and reliability analysis of stainless steel rebar embedded in fiber reinforced coral aggregate concrete. *Constr. Build. Mater.* **2022**, *350*, 128783. [CrossRef]
9. Huang, D.; Niu, D.; Li, S.; Zheng, H.; Fu, Q.; Liu, Y. Effects of mineral admixtures on chloride diffusion in environment-friendly coral aggregate concrete. *J. Renew. Mater.* **2022**, *10*, 3477. [CrossRef]
10. Ma, L.; Li, Z.; Wang, M.; Wei, H.; Fan, P. Effects of size and loading rate on the mechanical properties of single coral particles. *Powder Technol.* **2019**, *342*, 961–971. [CrossRef]
11. Zhang, J.; Wu, Z.; Zhang, Y.; Fang, Q.; Yu, H.; Jiang, C. Mesoscopic characteristics and macroscopic mechanical properties of coral aggregates. *Constr. Build. Mater.* **2021**, *309*, 125125. [CrossRef]
12. Wang, A.; Zhang, Z.; Liu, K.; Xu, H.; Shi, L.; Sun, D. Coral aggregate concrete: Numerical description of physical, chemical and morphological properties of coral aggregate. *Cem. Concr. Compos.* **2019**, *100*, 25–34. [CrossRef]
13. Zhang, P.; Zheng, Y.; Wang, K.; Zhang, J. A review on properties of fresh and hardened geopolymer mortar. *Compos. Part B Eng.* **2018**, *152*, 79–95. [CrossRef]
14. Van Jaarsveld, J.G.S.; Van Deventer, J.S.J.; Lorenzen, L. The potential use of geopolymeric materials to immobilise toxic metals: Part I. Theory and applications. *Miner. Eng.* **1997**, *10*, 659–669. [CrossRef]
15. Zhang, B.; Zhu, H.; Lu, F. Fracture properties of slag-based alkali-activated seawater coral aggregate concrete. *Theor. Appl. Fract. Mech.* **2021**, *115*, 103071. [CrossRef]
16. Zhang, B.; Zhu, H.; Shah, K.W.; Dong, Z.; Wu, J. Performance evaluation and microstructure characterization of seawater and coral/sea sand alkali-activated mortars. *Constr. Build. Mater.* **2020**, *259*, 120403. [CrossRef]
17. Zhang, B.; Zhu, H.; Shah, K.W.; Dong, Z.; Wu, J. Design and properties of seawater coral aggregate alkali-activated concrete. *J. Sustain. Cem.-Based Mater* **2022**, *11*, 187–201. [CrossRef]
18. Wu, W.; Wang, R.; Zhu, C.; Meng, Q. The effect of fly ash and silica fume on mechanical properties and durability of coral aggregate concrete. *Constr. Build. Mater.* **2018**, *185*, 69–78. [CrossRef]
19. Yuan, J.; Ou, Z. Research progress and engineering applications of stainless steel-reinforced concrete structures. *Adv. Civ. Eng.* **2021**, *2021*, 9228493. [CrossRef]
20. Jing, Q.; Fang, X.; Ni, J.; Tang, Y.; Fang, X. Use of 2304 Stainless steel reinforcement in Hong Kong-Zhuhai-Macau bridge-corrosion behaviours of 2304 stainless steel reinforcement. *J. Highw. Transp. Res. Dev.* **2017**, *34*, 51–56.
21. Da, B.; Yu, H.F.; Ma, H.Y.; Wu, Z. Anti-corrosion performances of different types of rebars in coral aggregate seawater concrete. *Mater. Rep.* **2019**, *33*, 2002–2008. (In Chinese)
22. Li, Q.; Kuang, Y.; Guo, W.; Zhang, Y. Experimental research on mechanical performance of SSRC columns under eccentric compression. *Appl. Sci.* **2020**, *10*, 5629. [CrossRef]

23. Rabi, M.; Cashell, K.A.; Shamass, R. Flexural analysis and design of stainless steel reinforced concrete beams. *Eng. Struct.* **2019**, *198*, 109432. [CrossRef]
24. Geromel, M.; Mazzarella, O. Experimental and analytical assessment of the behavior of stainless steel reinforced concrete beams. *Mater. Struct.* **2005**, *38*, 211–218. [CrossRef]
25. Li, Q.; Guo, W.; Liu, C.; Kuang, Y.; Geng, H. Experimental and theoretical studies on flexural performance of stainless steel reinforced concrete beams. *Adv. Civ. Eng.* **2020**, *2020*, 4048750. [CrossRef]
26. Rabi, M.; Cashell, K.A.; Shamass, R. Ultimate behaviour and serviceability analysis of stainless steel reinforced concrete beams. *Eng. Struct.* **2021**, *248*, 113259. [CrossRef]
27. Khalifa, M. Heat of Hydration Thermal Performance and Flexural Capacity of Stainless-Steel Reinforced Concrete Sections. Master's Thesis, The University of Western Ontario (Canada), London, ON, Canada, 2019.
28. Zhang, G.; Zhang, Y.; Zhou, Y. Fatigue tests of concrete slabs reinforced with stainless steel bars. *Adv. Mater. Sci. Eng.* **2018**, *2018*, 5451398. [CrossRef]
29. Fu, J.; Ge, X.; Li, J.; Sun, Z.; Wang, D. Seismic performance of concrete bridge piers reinforced by stainless steel bars: A quasi-static experimental study. *Eng. Struct.* **2022**, *266*, 114507. [CrossRef]
30. Nicoletti, V.; Carbonari, S.; Gara, F. Nomograms for the pre-dimensioning of RC beam-column joints according to Eurocode 8. *Structures* **2022**, *39*, 958–973. [CrossRef]
31. Zhou, Y.J.; Wang, X.T.; Sun, H.R.; Chen, X.; Wang, T. Residual seismic performance for damaged RC frame based on beam-to-column joint subassemblies. *Structures* **2025**, *71*, 107980. [CrossRef]
32. *JGJ51-2002*; Technical Code for Lightweight Aggregate Concrete. China Architecture & Building Press: Beijing, China, 2002. (In Chinese)
33. *GB/T17431-2010*; Lightweight Aggregate and Its Test Methods. Standards Press of China: Beijing, China, 2010. (In Chinese)
34. *JGJ52-2006*; Standard for Quality and Testing Methods of Sand and Crushed Stone for Ordinary Concrete. China Architecture & Building Press: Beijing, China, 2006. (In Chinese)
35. Liu, B.; Ye, J.; Liu, X.; Lin, W.; Deng, Z.; Liu, Q. Shear strength and failure criterion of carbon fiber reinforced coral concrete under combined compression-shear stresses. *Constr. Build. Mater.* **2022**, *325*, 126728. [CrossRef]
36. *GB/T228.1-2021*; Tensile Testing of Metallic Materials-Part 1: Room Temperature Test Method. Standards Press of China: Beijing, China, 2021. (In Chinese)
37. Deng, M.; Pan, J.; Liang, X. Uniaxial compressive test of high ductile fiber-reinforced concrete and damage constitutive model. *Adv. Civ. Eng.* **2018**, *2018*, 4308084. [CrossRef]
38. Liu, B.; Zhou, J.; Wen, X.; Hu, X.; Deng, Z. Mechanical properties and constitutive model of carbon fiber reinforced coral concrete under uniaxial compression. *Constr. Build. Mater.* **2020**, *263*, 120649. [CrossRef]
39. Da, B.; Chen, Y.; Yu, H.; Ma, H.; Chen, D.; Wu, Z.; Liu, J.; Li, Y. Preparation technology, mechanical properties and durability of coral aggregate seawater concrete in the island-reef environment. *J. Clean. Prod.* **2022**, *339*, 130572. [CrossRef]
40. *GB50010-2010*; Code for Design of Concrete Structures. China Architecture & Building Press: Beijing, China, 2015. (In Chinese)
41. *JGJ12-2006*; Technical Code for Lightweight Aggregate Concrete Structures. China Architecture & Building Press: Beijing, China, 2006. (In Chinese)
42. *GB50068-2018*; Unified Standard for Reliability Design of Engineering Structures. China Architecture & Building Press: Beijing, China, 2018. (In Chinese)